



# Assembly of COFs layer and electron mediator on silica for visible light driven photocatalytic NADH regeneration

Jiali Liu <sup>a,b</sup>, Xiaomin Ren <sup>a,b</sup>, Chunzhi Li <sup>a,b</sup>, Maodi Wang <sup>a,b</sup>, He Li <sup>a,\*</sup>, Qihua Yang <sup>a,\*</sup>

<sup>a</sup> State Key Laboratory of Catalysis, Dalian Institute of Chemical Physics, Chinese Academy of Sciences, 457 Zhongshan Road, Dalian 116023, China

<sup>b</sup> University of Chinese Academy of Sciences, 19A Yuquan Road, Shijingshan District, Beijing 100049, China



## ARTICLE INFO

**Keywords:**  
Photocatalysis  
NADH regeneration  
COFs  
Electron mediator  
Thin layer

## ABSTRACT

Photocatalytic regeneration of the high-cost co-factor NADH is a promising method to couple photo-enzyme catalysis, however, the usage of homogeneous electron mediator ( $[Cp^*Rh(bpy)H_2O]^{2+}$ ) which deactivates enzymes deteriorates the whole process efficiency. Herein, we report the immobilization of electron mediator ( $[Cp^*Rh(bpy)H_2O]^{2+}$ ) on covalent organic frameworks (COFs) by the sequential assembly method. The resultant bi-functional photocatalyst with controlled cascade electron transfer afforded NADH production rate of  $9.8 \text{ mmol}\cdot\text{g}_{\text{COF}}^{-1}\cdot\text{h}^{-1}$ , much higher than previously reported ones with integrated electron mediator. The photo-enzyme coupling system with the photocatalyst and alcohol dehydrogenase could continuously produce butanol for at least 180 min under visible light irradiation, implying the potential application of bi-functional photocatalyst in artificial photosynthesis.

## 1. Introduction

NADH (reduced form of nicotinamide adenine dinucleotide) is a widely used cofactor for most reductases, e.g., alcohol dehydrogenases, amino-acid dehydrogenases, transhydrogenases, peroxidases and reductive dehalogenases [1–3]. Due to its high price, in situ NADH regeneration is required for industrial applications of enzymatic catalysis involving reductases [4,5]. Up to date, chemical reduction [6], homogeneous catalytic reduction [7,8], heterogeneous catalytic reduction [9–11], enzymatic reduction [12], electrochemical reduction [13–15] and photocatalytic reduction [16,17] have been developed for NADH regeneration. Among them, photocatalytic regeneration of NADH has attracted a lot of research attention in recent years due to the usage of clean and sustainable solar energy and the importance of the artificial photosynthesis. Different types of semiconductors have been tested in photocatalytic regeneration of NADH including TiO<sub>2</sub> [18], CdS [19], C<sub>3</sub>N<sub>4</sub> [20–22], metal-organic frameworks (MOFs) [23,24] and covalent organic frameworks (COFs) [25–29]. However, the efficient photocatalysts with wide visible light absorbance, suitable band structure, high apparent quantum efficiency and high stability is still rare.

Recently, 2-D COFs has emerged as a potential type of organic semiconductors for photocatalysis [30–33]. In comparison with inorganic semiconductors, 2-D COFs have the advantages of strong visible

light absorption and facile band structure engineering due to the easy composition variation by weaving chemistry. In addition to photocatalytic CO<sub>2</sub> reduction [34,35], H<sub>2</sub> evolution [36–38], and organic transformation reactions (such as selective oxidation [32,33,39,40] and cross-coupling [41]), 2-D COFs have also been used for photocatalytic NADH regeneration. For example, by using triazine-based 2D TFP-PDAN COFs with sp<sup>2</sup>-carbon linkages, Zhao and co-workers reported the NADH regeneration with a rate of about  $7.5 \text{ mmol}\cdot\text{g}^{-1}\cdot\text{h}^{-1}$  [25]. Thereafter, the same group converted imine-linked COFs into an ultra-stable and fully π-conjugated thieno[3,2-c]pyridine-linked 2D COFs and reached a very high rate of about  $9.3 \text{ mmol}\cdot\text{g}^{-1}\cdot\text{h}^{-1}$  for NADH regeneration [26]. Singh et al. reported a rate of  $1.6 \text{ mmol}\cdot\text{g}^{-1}\cdot\text{h}^{-1}$  for NADH regeneration with imine COFs [28]. More recently, we reported that the heteropolyacid/nano-TPTTA COFs composites with only 0.6 wt % TPTTA COFs gave 91% yield in 1 h for the photocatalytic NADH regeneration and the production rate of NADH reached up to  $72.0 \text{ mmol}\cdot\text{g}_{\text{COF}}^{-1}\cdot\text{h}^{-1}$  under visible light illumination [29].

$[Cp^*Rh(bpy)H_2O]^{2+}$  (abbreviated as M) is generally used as electron mediator to facilitate the two electrons coupled proton transfer involved in the photocatalytic NADH regeneration [17]. In most cases, M was added directly to the reaction solution and the recycling of the expensive M is tedious. Furthermore, the free M in the solution deactivates enzymes under illumination by binding to its amino acid-residues [42].

\* Corresponding authors.

E-mail addresses: [lihe@dicp.ac.cn](mailto:lihe@dicp.ac.cn) (H. Li), [yangqh@dicp.ac.cn](mailto:yangqh@dicp.ac.cn) (Q. Yang).

The integration of **M** with photocatalysts could help to solve the above problems. Zhang et al. reported no enzyme was deactivated from the attack of light-induced holes and **M** during the photo-enzyme coupling catalysis by embedding **M** in TiO<sub>2</sub> coated GCN [42]. Farha's group also demonstrated that NU-1006 installed with **M** gave 28% NADH regeneration yield in 2 h under white light [23]. It is also reported by Tian and co-workers that TPE-C<sub>3</sub>N<sub>4</sub> with integrated **M** gave a yield of 28% in 30 min in the photocatalytic NADH regeneration [21]. In comparison with the photocatalytic system using homogeneous **M**, the activity of the photocatalysts with integrated **M** is still very low.

As compared with inorganic semiconductors, the functionalization of COFs is more facile considering the predesign ability of COF structures. The COFs with bipyridine groups integrated in the framework have been previously reported [34,41,43–45]. Thus, the bipyridine-COFs are desirable platform materials for immobilization of **M**. However, bipyridine-COFs coordinated with **M** afforded very low activity in NADH regeneration possibly due to the difficulty in charge separation. Thus, the integration of bipyridine-COFs with other COFs possessing high charge separation efficiency is a good choice. But it is still a challenge to control the charge migration direction among different types of COFs. Our previous studies showed that COFs with different layer thickness could be facilely deposited on solid supports (SiO<sub>2</sub>, TiO<sub>2</sub>, CdS) by using COFs colloids, thereby the sequential deposition of different COFs colloid on the support could not only control the alternative local of different types of COFs but also manipulate the charge transfer direction [37].

Inspired by previous results, we report in this work the deposition of TPTTA COFs on SiO<sub>2</sub> nanospheres (SiO<sub>2</sub> nanospheres were chosen considering its inertness in photocatalysis) for photocatalytic NADH regeneration with an aim to accelerate the charge separation efficiency and reduce the amounts of expensive COFs. The optimized composite photocatalyst achieved a NADH production rate of 55.6 mmol·g<sub>COF</sub><sup>-1</sup>·h<sup>-1</sup>. The following deposition of bipyridine functionalized TPBpy layer realized the immobilization of **M** on the composite photocatalyst and reached a photocatalytic NADH production rate of 9.8 mmol·g<sub>COF</sub><sup>-1</sup>·h<sup>-1</sup>. The influence of COF layer thickness and the electron transfer efficiency on the photocatalytic activity was also investigated.

## 2. Experimental section

### 2.1. Materials

All reagents were of analytical grade and used without further purification. 1,3,5-Triformylphloroglucinol (TP), 4,4',4''-(1,3,5-triazine-2,4,6-triyl) trianiline (TTA) and 2,2'-bipyridine-5,5'-diamine (Bpy) were purchased from Jilin Province Extension Technology Co. Sodium dodecyl sulfate (SDS), KH<sub>2</sub>PO<sub>4</sub> and K<sub>2</sub>HPO<sub>4</sub> were purchased from Sinopharm Chemical Reagent Co., Ltd. Hexadecyl trimethyl ammonium bromide (CTAB) was purchased from J&K Scientific Ltd. SiO<sub>2</sub> colloid solution (LUDOX TM-40 colloidal silica) was bought from Aldrich Co., Ltd, of which the density is 1.3 g/mL with 40 wt% SiO<sub>2</sub>.  $\beta$ -Nicotinamide adenine dinucleotide (NAD<sup>+</sup>),  $\beta$ -nicotinamide adenine dinucleotide reduced disodium salt hydrate (NADH) and n-butanal were purchased from Aladdin Reagent Company. Alcohol dehydrogenase and glucose dehydrogenase were obtained from Yuanye Biology (Shanghai). Nano-TPTTA COF, TPTTA COFs colloids, TPTTA<sub>x</sub>/SiO<sub>2</sub> and [Cp<sup>\*</sup>Rh(bpy)H<sub>2</sub>O]<sup>2+</sup> (abbreviated as **M**) were synthesized according to the literature procedure [25,37].

### 2.2. Characterizations

Dynamic light scattering (DLS) analysis was performed on the Malvern Zetasizer Nano ZS90 analyzer. The Ar adsorption-desorption experiments were performed at 87 K using a Quantachrome Autosorb iQ. Transmission electron microscopy (TEM) images were carried out on a Hitachi 7700, at an acceleration voltage of 100 kV. Scanning electron

microscopy (SEM) was undertaken by using a JSM 7900 apparatus operating at an acceleration voltage of 1 kV. Scanning transmission electron microscopy (STEM) was undertaken on a JEM-F200 operating at an acceleration voltage of 1–20 kV. FT-IR spectra in the range of 400–4000 cm<sup>-1</sup> were collected with a Nicolet Nexus iS50 IR spectrometer using KBr pellets. Liquid <sup>1</sup>H NMR spectra were recorded on a Bruker Advance 400 MHz spectrometer. Solid-state <sup>13</sup>C CP TOSS (total suppression of spinning sidebands) spectrum was tested on a Bruker 600 MHz spectrometer. Inductively coupled plasma atomic emission spectrometry (ICP) was determined by PLASAM-SPEC-II instrument. X-ray photoelectron spectroscopy (XPS) experiments were tested on a Kratos AXIS HSi spectrometer equipped with a monochromated Al K $\alpha$  source (1486.7 eV) and a charge neutralizer.

## 2.3. Preparation

### 2.3.1. Preparation of nano-TPBpy COFs colloids

Typically, 12.6 mg (0.06 mmol) TP and 16.8 mg (0.09 mmol) Bpy were dissolved in 0.25 mL DMSO respectively and added dropwise to a flask containing 58 mL of 0.1 M CTAB aqueous solution and 1.8 mL of 0.1 M SDS aqueous solution separately. After the suspensions were fully ultrasonicated, the two obtained solutions were mixed. After reacting at 30 °C for 72 h, nano-TPBpy COF colloids was obtained.

### 2.3.2. Preparation of nano-TPBpy COFs

Typically, 6.8 mL of ammonia solution and 100 mL ethanol were added to the above TPBpy COFs colloid solution. The crimson nano-TPBpy COF powder was obtained by centrifugation, washed thoroughly with ethanol and dried in vacuum for 6 h at room temperature.

### 2.3.3. Preparation of TPTTA<sub>x</sub>@TPBpy<sub>y</sub>/SiO<sub>2</sub>

600 mg of TPTTA<sub>5</sub>/SiO<sub>2</sub> was added to 21.7 mL of nano-TPBpy COFs solution. After fully sonicating, the suspension was stirred at 30 °C for two days and the aqueous solution was evaporated at 110 °C. The TPTTA<sub>5</sub>@TPBpy<sub>0.75</sub>/SiO<sub>2</sub> was obtained by washing thoroughly with ethanol and drying in vacuum for 6 h at room temperature.

The TPTTA<sub>5</sub>@TPBpy<sub>0.5</sub>/SiO<sub>2</sub> and TPTTA<sub>5</sub>@TPBpy<sub>1.5</sub>/SiO<sub>2</sub> were synthesized in a method similar to TPTTA<sub>5</sub>@TPBpy<sub>0.75</sub>/SiO<sub>2</sub> with the exception that 900 mg and 300 mg TPTTA<sub>5</sub>/SiO<sub>2</sub> were used respectively.

### 2.3.4. Preparation of TPTTA<sub>x</sub>@TPBpy<sub>y</sub>Rh/SiO<sub>2</sub> and nano-TPBpy-Rh

Desired amount of methanol solution of [Cp<sup>\*</sup>RhCl<sub>2</sub>]<sub>2</sub> (6 mM) and 300 mg TPTTA<sub>x</sub>@TPBpy<sub>y</sub>/SiO<sub>2</sub> or nano-TPBpy were mixed in a flask. For TPTTA<sub>5</sub>@TPBpy<sub>0.5</sub>/SiO<sub>2</sub>, TPTTA<sub>5</sub>@TPBpy<sub>0.75</sub>/SiO<sub>2</sub>, TPTTA<sub>5</sub>@TPBpy<sub>1.5</sub>/SiO<sub>2</sub> and nano-TPBpy, the volume of the added [Cp<sup>\*</sup>RhCl<sub>2</sub>]<sub>2</sub> methanol solution was 0.9, 1.35, 2.7 and 18 mL, respectively. After stirring the mixture at room temperature for 12 h, the solid product was separated by centrifugation, washed with methanol and dichloromethane and dried under vacuum to afford TPTTA<sub>x</sub>@TPBpy<sub>y</sub>-Rh/SiO<sub>2</sub> or nano-TPBpy-Rh.

### 2.3.5. Preparation of TPBpy<sub>0.75</sub>-Rh@TPTTA<sub>5</sub>/SiO<sub>2</sub>

TPBpy<sub>0.75</sub>-Rh@TPTTA<sub>5</sub>/SiO<sub>2</sub> was prepared in a similar method to TPTTA<sub>5</sub>@TPBpy<sub>y</sub>-Rh/SiO<sub>2</sub> except that the deposition process is reversed (Scheme S1).

## 2.4. Photocatalytic NADH regeneration

Typically, 15 mg of photocatalyst, 1 mM NAD<sup>+</sup> and 2.6 mL of PBS buffer (pH = 8, TEOA 15 w/v%) were added into a 10 mL quartz reactor. The suspension was sonicated for 10 min and fully degassed. The photocatalytic NADH regeneration was performed using a 300 W Xe lamp (Ushio-CERMAX LX300) with optical cutoff filter (kenko, L42;  $\lambda \geq 420$  nm). The regeneration yield of NADH was analyzed by UV-vis spectroscopy.

Since SiO<sub>2</sub> and TPBPy-Rh had no contribution to the photocatalytic

activity, the TOF was normalized with the content of TPTTA COFs and calculated at NAD<sup>+</sup> conversion less than 30% according to the following formula.

$$TOF = \frac{n_{NAD^+}}{M_{COF} \times t}$$

$n_{NAD^+}$ : converted NAD<sup>+</sup> (mmol).

M<sub>COF</sub>: mass of TPTTA in photocatalyst (g).  
t: reaction time (h).

### 2.5. Coupling photocatalytic NADH regeneration and enzymatic reduction of n-butanal and benzaldehyde

For n-butanal, 15 mg of TPTTA<sub>5</sub>@TPBpy<sub>0.75</sub>-Rh/SiO<sub>2</sub>, 30 U ADH solution (15 kU/mL), 1.9 mg (3 μmol) NAD<sup>+</sup> and 1.3 mL of PBS buffer (pH = 8, containing 0.3 g of TEOA) were added into a 10 mL quartz reactor and the suspension was sonicated for 10 min and fully degassed. After that, 1.3 mL of degassed PBS buffer (pH = 8, containing 0.3 g of TEOA and 10 mg of n-butanal) was added into the reactor. The suspension was illuminated by a 300 W Xe lamp (Ushio-CERMAX LX300) with optical cutoff filter (kenko, L42;  $\lambda \geq 420$  nm). The content of 1-butanol was analyzed by gas chromatography with a PEG column.

The similar procedure was used for the reduction of benzaldehyde with the exception that 100 mg of benzaldehyde and 0.5 mL acetonitrile were added.

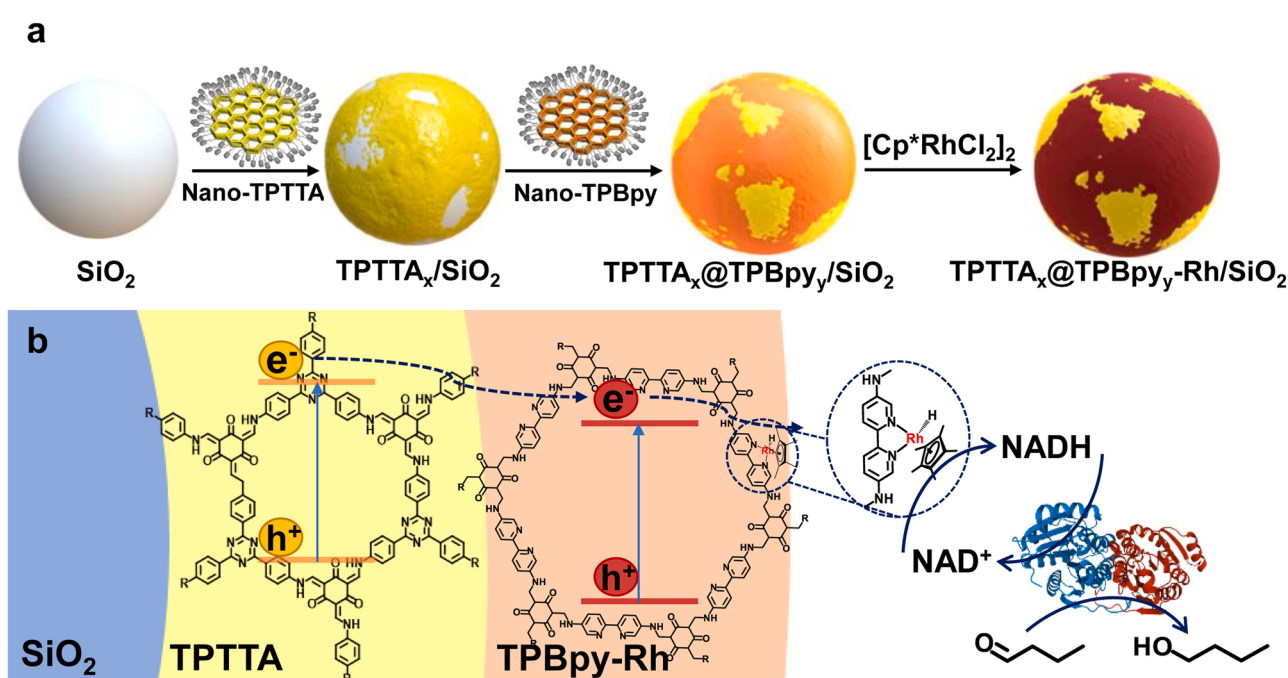
## 3. Results and discussion

### 3.1. Preparation and characterizations of the composite photocatalysts with COF layers supported on SiO<sub>2</sub>

Previously we reported the deposition of 2-D COFs colloids on solid supports e.g., SiO<sub>2</sub>, TiO<sub>2</sub> and CdS [37]. In comparison with conventional solvothermal method, the deposition of COF colloids provides a facile method to support COFs with different layer thickness on solid materials. For preparation of the composite materials with controlled location of different COFs, the sequential deposition method was used

(Scheme 1). In the first step, the TPTTA<sub>x</sub>/SiO<sub>2</sub> samples (x denotes weight percent of TPTTA colloids in the initial preparation mixture, TPTTA structure see Scheme 1b) with different COFs layer thickness were prepared by mixing TPTTA colloids and commercial SiO<sub>2</sub> nanospheres (particle size ~26 nm) followed by solvent evaporation according to our previous report (Scheme 1a) [37]. The TPTTA colloids with size of ~33 nm measured by dynamic light scattering (DLS) method (Fig. S1) were obtained by condensation of 1,3,5-triformylphloroglucinol (TP) and 4,4',4''-(1,3,5-triazine-2,4,6-triyl) trianiline (TTA) in the confined space of cationic hexadecyltrimethylammonium bromide (CTAB) and anionic sodium dodecyl sulfate (SDS) surfactants micelles. The transmission electron microscope (TEM) and scanning electron microscopy (SEM) images of TPTTA<sub>x</sub>/SiO<sub>2</sub> were identical to parent SiO<sub>2</sub> nanospheres and no impurity of COFs aggregates could be observed, implying the distribution of TPTTA layer on SiO<sub>2</sub> nanospheres, consistent with our previous report (Fig. S2) [37]. The STEM image and corresponding EDS elemental mapping of representative TPTTA<sub>10</sub>/SiO<sub>2</sub> shows the uniform distribution of Si and C element, further confirming the deposition of TPTTA on SiO<sub>2</sub> (Fig. S3). Furthermore, the TPTTA thickness on SiO<sub>2</sub> was 1.0 nm and 3.8 nm respectively for TPTTA<sub>5</sub>/SiO<sub>2</sub> and TPTTA<sub>10</sub>/SiO<sub>2</sub> calculated by small angle X-ray scattering result (SAXS) (Fig. S4, details see SI). The TPTTA contents measured by <sup>1</sup>H NMR analysis of the digested sample in KOH varied from 1.2 to 9.9 wt% (Table 1, details see Fig. S5), very similar to the TPTTA contents in the initial mixture. This implies the almost complete deposition of TPTTA on SiO<sub>2</sub>. The control sample, TPTTA<sub>5-E</sub>/SiO<sub>2</sub> was prepared in a similar method to TPTTA<sub>5</sub>/SiO<sub>2</sub> with the exception that the solvent evaporation method was replaced by the ethanol precipitation strategy. The SEM image of this sample displayed the co-existence of COFs aggregates and SiO<sub>2</sub> nanospheres (Fig. S6), implying that TPTTA cannot be well supported on SiO<sub>2</sub> by ethanol precipitation method. Another control sample nano-TPTTA COF was prepared by precipitation of TPTTA colloid solution with ethanol. The SEM image showed that nano-TPTTA COF was composed of agglomerated particles (Fig. S7).

To immobilize M ( $[Cp^*Rh(bpy)H_2O]^{2+}$ ), TPBpy colloids were prepared using 1,3,5-triformylphloroglucinol (TP) and 2,2'-bipyridine-5,5'-diamine (Bpy) as monomers with the aid of CTAB/SDS micelle in a



**Scheme 1.** Illustration for (a) preparation of TPTTA<sub>x</sub>/SiO<sub>2</sub>, TPTTA<sub>x</sub>@TPBpy<sub>y</sub>/SiO<sub>2</sub>, and TPTTA<sub>x</sub>@TPBpy<sub>y</sub>-Rh/SiO<sub>2</sub> photocatalyst by sequential deposition method (Yellow color refers to TPTTA COF, the orange color refers to TPBpy COF and the russet color refers to TPBpy-Rh) and (b) cascade electron transfer in TPTTA<sub>x</sub>@TPBpy<sub>y</sub>-Rh/SiO<sub>2</sub> during photocatalytic NADH regeneration and photo-enzymatic butanol production.

**Table 1**Chemical composition and textural parameters of composite materials and photocatalytic NADH regeneration with  $\text{TPTTA}_x@\text{TPBpy}_y\text{-Rh/SiO}_2$  and  $\text{TPTTA}_x/\text{SiO}_2$ .<sup>a</sup>

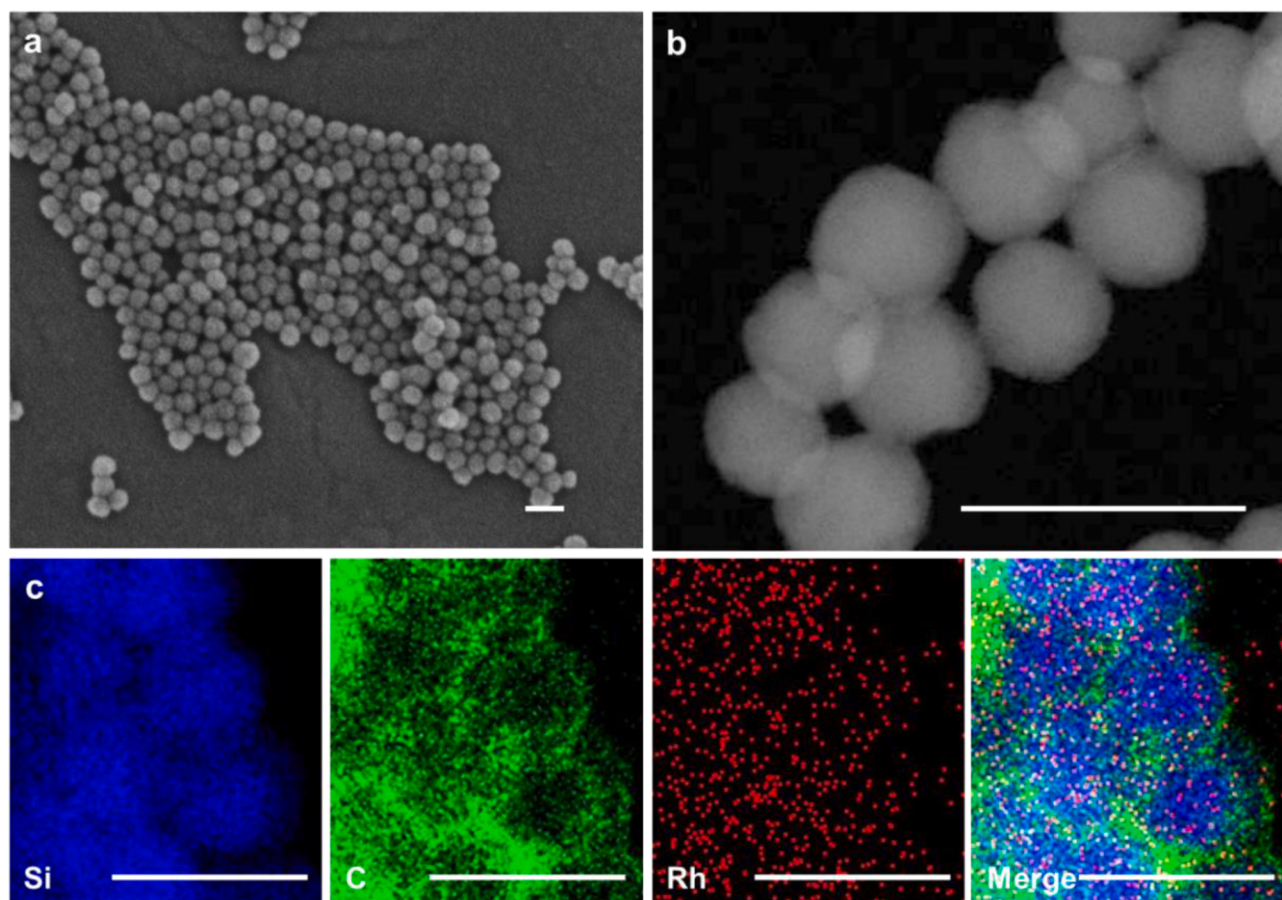
Photocatalyst	TPTTA content (wt%)	TPBpy content (wt%)	Rh (wt%)	BET SSA ( $\text{m}^2/\text{g}$ )	<b>M</b>	Yield (%)	TOF (mmol·g <sub>COF</sub> <sup>-1</sup> ·h <sup>-1</sup> )
$\text{TPTTA}_1/\text{SiO}_2$	1.2	–	–	128	+	73	55.6
$\text{TPTTA}_5/\text{SiO}_2$	5.1	–	–	141	+	88	14.2
$\text{TPTTA}_{10}/\text{SiO}_2$	9.9	–	–	175	+	72	5.6
$\text{TPBpy}_{0.75}\text{-Rh/SiO}_2$	–	0.7	0.6	115	–	0	0
$\text{TPTTA}_5@\text{TPBpy}_{0.5}\text{-Rh/SiO}_2$	4.7	0.5	0.28	202	–	47	5.7
$\text{TPTTA}_5@\text{TPBpy}_{0.75}\text{-Rh/SiO}_2$	4.7	0.7	0.42	188	–	69	9.8
$\text{TPTTA}_5@\text{TPBpy}_{1.5}\text{-Rh/SiO}_2$	4.6	1.5	0.85	139	–	58	4.3
Nano-TPTTA <sup>b</sup>	–	–	–	–	+	51	0.9
$\text{TPBpy}_{0.75}\text{-Rh/TPTTA}_5/\text{SiO}_2$	4.8	0.8	0.6	368	–	14	1.0
$\text{TPBpy}_{0.75}\text{-Rh/SiO}_2 + \text{TPTTA}_5/\text{SiO}_2$	–	–	–	–	–	36	2.2
$\text{TPTTA}_5@\text{TPBpy}_{0.75}/\text{SiO}_2$ <sup>c</sup>	4.8	0.7	–	–	+	63	7.4

<sup>a</sup> Reaction conditions: photocatalyst (15 mg),  $\text{NAD}^+$  (1 mM), **M** (0.25 mM), 2.1 mL of Phosphate buffer (pH = 8), TEOA (15 w/v %),  $\lambda \geq 420$  nm, 40 min<sup>b</sup> 3 mg of Nano-TPTTA was used.<sup>c</sup> The amount of **M** for  $\text{TPTTA}_5@\text{TPBpy}_{0.75}/\text{SiO}_2$  was the same with that of  $\text{TPTTA}_5@\text{TPBpy}_{0.75}\text{-Rh/SiO}_2$ .

similar way to TPTTA colloids. The DLS measurement showed that the TPBpy colloid size was ~42 nm and the Tyndall effect further confirmed the formation of colloid (Fig. S1). The FT-IR spectrum of nano-TPBpy COFs obtained by ethanol precipitation of TPBpy colloids displayed the vibration peaks of the keto-formate at  $1579\text{ cm}^{-1}$  ( $\text{C}=\text{C}$ ) and  $1624\text{ cm}^{-1}$  ( $\text{C}=\text{O}$ ), implying the formation of  $\beta$ -ketoenamine linkage between TP and Bpy (Fig. S8) [46]. Furthermore, the C-N vibration at  $1266\text{ cm}^{-1}$  derived from Bpy confirmed the existence of Bpy. The SEM image showed that nano-TPBpy COF was composed of agglomerated particles, similar to nano-TPTTA COF (Fig. S7). Then, TPBpy colloids were deposited on  $\text{TPTTA}_5/\text{SiO}_2$  by solvent evaporation method to obtain  $\text{TPTTA}_5@\text{TPBpy}_y/\text{SiO}_2$  ( $y$  denotes weight percent of TPBpy colloids in the initial preparation mixture). Choosing  $\text{TPTTA}_5/\text{SiO}_2$  was

based on its high yield in photocatalytic NADH regeneration in the presence of homogeneous **M** discussed later. Finally, **M** was fixed on  $\text{TPTTA}_5@\text{TPBpy}_y/\text{SiO}_2$  through the coordination of  $(\text{Cp}^*\text{RhCl}_2)_2$  and the bipyridine group of TPBpy to afford  $\text{TPTTA}_5@\text{TPBpy}_y\text{-Rh/SiO}_2$  (Scheme 1b). A control sample  $\text{TPBpy}_{0.75}\text{-Rh/SiO}_2$  was prepared by deposition of TPBpy colloid on  $\text{SiO}_2$  spheres followed by coordination with  $(\text{Cp}^*\text{RhCl}_2)_2$ . The control sample  $\text{TPBpy}_{0.75}\text{-Rh/TPTTA}_5/\text{SiO}_2$  was prepared in a similar method to  $\text{TPTTA}_5@\text{TPBpy}_{0.75}\text{-Rh/SiO}_2$  except that the deposition process is reversed.

The SEM and TEM images of all  $\text{TPTTA}_5@\text{TPBpy}_y\text{-Rh/SiO}_2$  samples clearly showed nanospherical morphology (~28 nm in size) (Fig. 1a and S6), implying the successfully deposition of TPBpy on  $\text{TPTTA}_5/\text{SiO}_2$  which is possibly driven by Vander Waals force between TPTTA and

**Fig. 1.** (a) SEM, (b) STEM image and (c) corresponding EDS elemental mapping of  $\text{TPTTA}_5@\text{TPBpy}_{0.75}\text{-Rh/SiO}_2$  (scale bar: 50 nm).

TPBpy. No significant difference in particle size of TPTTA<sub>5</sub>@TPBpy<sub>y</sub>-Rh/SiO<sub>2</sub> and TPTTA<sub>x</sub>/SiO<sub>2</sub> could be observed, suggesting that the TPBpy-Rh layer on the material was ultrathin. The scanning transmission electron microscopy (STEM) image of representative TPTTA<sub>5</sub>@TPBpy<sub>0.75</sub>-Rh/SiO<sub>2</sub> further confirmed the nano-spherical morphology (Fig. 1b), consistence with the SEM and TEM results. The uniform distribution of Si, C and Rh elements as well as the merged image detected by energy-dispersive X-ray spectroscopy (EDS) elemental mapping further revealed the close contact of Si, C and Rh, showing the well distribution of COFs layers and Rh on SiO<sub>2</sub> (Fig. 1c).

The TPTTA and TPBpy content of TPTTA<sub>5</sub>@TPBpy<sub>y</sub>/SiO<sub>2</sub> and control samples was analyzed by <sup>1</sup>H NMR of the digested sample (Table 1, Fig. S5). The contents of TPBpy in TPTTA<sub>5</sub>@TPBpy<sub>0.5</sub>/SiO<sub>2</sub>, TPTTA<sub>5</sub>@TPBpy<sub>0.75</sub>/SiO<sub>2</sub>, TPTTA<sub>5</sub>@TPBpy<sub>1.5</sub>/SiO<sub>2</sub>, TPBpy<sub>0.75</sub>-Rh/SiO<sub>2</sub> and TPBpy<sub>0.75</sub>-Rh/TPTTA<sub>5</sub>/SiO<sub>2</sub> was 0.5, 0.7, 1.5, 0.7 and 0.8 wt% respectively, similar to the contents of TPBpy colloids in the initial mixture. The almost complete deposition of TPBpy colloid shows the efficiency of this method for preparation of composite materials. As determined by inductively coupled plasma spectrometry, the Rh contents of TPTTA<sub>5</sub>@TPBpy<sub>y</sub>-Rh/SiO<sub>2</sub> increased from 0.28 to 0.85 wt% with the increase of the TPBpy contents. The FT-IR spectra of TPTTA<sub>x</sub>/SiO<sub>2</sub>, TPTTA<sub>5</sub>@TPBpy<sub>y</sub>/SiO<sub>2</sub> and TPTTA<sub>5</sub>@TPBpy<sub>y</sub>-Rh/SiO<sub>2</sub> samples all displayed the characteristic vibration peaks at 1579 cm<sup>-1</sup>, 1624 cm<sup>-1</sup> and 1510 cm<sup>-1</sup> assigned respectively to C=C, C=O stretching vibrations and the vibration from triazine ring implying the formation of  $\beta$ -ketoenamine linked COFs (Fig. 2a and S8). The absence of characteristic vibrations of CTAB and SDS revealed the almost complete removal of surfactants by washing step. The <sup>13</sup>C CP-TOSS NMR spectra of TPTTA<sub>10</sub>/SiO<sub>2</sub> and TPTTA<sub>5</sub>@TPBpy<sub>1.5</sub>/SiO<sub>2</sub> clearly show the characteristic peaks of C=O of the keto form and the C=N of triazine unites at 183 ppm and 169 ppm, respectively (Fig. S9). However, the characteristic peaks of Bpy cannot be clearly identified in FT-IR and <sup>13</sup>C CP-TOSS NMR spectra due to the low content of TPBpy and the interference of triazine ring (Fig. S8 and S9).

The textural structure of TPTTA<sub>5</sub>@TPBpy<sub>y</sub>-Rh/SiO<sub>2</sub> samples was measured by Ar sorption isotherms at 87 K. All samples exhibited IV isotherm pattern, resembling that of TPTTA<sub>5</sub>/SiO<sub>2</sub> (Fig. S10). The Brunauer-Emmett-teller (BET) surface area decreased as the TPBpy-Rh content increased (Table 1), which is related with the nonporous nature of nano-TPBpy-Rh (Fig. 2c). The BET surface area of TPTTA<sub>5</sub>@TPBpy<sub>1.5</sub>-Rh/SiO<sub>2</sub> was almost the same as that of the parent SiO<sub>2</sub>, much lower than those of TPTTA<sub>5</sub>@TPBpy<sub>0.5</sub>-Rh/SiO<sub>2</sub> and TPTTA<sub>5</sub>@TPBpy<sub>0.75</sub>-Rh/SiO<sub>2</sub>. As reported previously, the pore size distribution at 0.6 and 0.9 nm was from the TPTTA COF [37]. The pore size distribution of TPTTA<sub>5</sub>@TPBpy<sub>0.5</sub>-Rh/SiO<sub>2</sub> and TPTTA<sub>5</sub>@TPBpy<sub>0.75</sub>-Rh/SiO<sub>2</sub> was similar to that of TPTTA<sub>5</sub>/SiO<sub>2</sub> (Fig. 2c and S10), suggesting the incomplete coverage of the nonporous TPBpy-Rh layer on TPTTA<sub>5</sub>/SiO<sub>2</sub>. No micropores could be observed in the pore size distribution of TPTTA<sub>5</sub>@TPBpy<sub>1.5</sub>-Rh/SiO<sub>2</sub>, implying the complete coverage of TPTTA<sub>5</sub>/SiO<sub>2</sub> by TPBpy-Rh layer (Fig. 2c). To further confirm the

immobilization of M on TPTTA<sub>5</sub>@TPBpy<sub>y</sub>/SiO<sub>2</sub>, the X-ray photoelectron spectroscopy (XPS) was performed to investigate the chemical states of TPTTA<sub>5</sub>@TPBpy<sub>0.75</sub>-Rh/SiO<sub>2</sub>. As illustrated in Fig. S11, O1s, C1s, N1s, Si2p and Rh3d were detected in the survey spectra though the intensities of N1s and Rh3d peaks were weak due to the low content of TPBpy COF. The XPS Rh3d binding energies of TPTTA<sub>5</sub>@TPBpy<sub>0.75</sub>-Rh/SiO<sub>2</sub> were consistent with those of [Cp<sup>\*</sup>Rh(bpy)H<sub>2</sub>O]<sup>2+</sup> reported in the literature (Fig. 2b) [21,42], implying the similar chemical structure of M before and after immobilization. The results above confirm the successful immobilization of M in the photocatalyst with the sequential deposition method.

### 3.2. Optical electronic properties

The UV-vis diffusion reflectance spectra show strong visible light responsive property of TPTTA<sub>x</sub>/SiO<sub>2</sub> and TPTTA<sub>5</sub>@TPBpy<sub>y</sub>-Rh/SiO<sub>2</sub> (Fig. 3a and S12). The absorption edges of TPTTA<sub>x</sub>/SiO<sub>2</sub> gradually blue shifted with the decrease of the content of TPTTA COF, which is reasonable due to the less conjugate structure with decreasing thickness of TPTTA layer. In comparison with TPTTA<sub>5</sub>/SiO<sub>2</sub>, the absorption edge of TPTTA<sub>5</sub>@TPBpy<sub>y</sub>-Rh/SiO<sub>2</sub> red shifted due to the presence of TPBpy-Rh. The blue shift in the adsorption edge of TPTTA<sub>5</sub>@TPBpy<sub>y</sub>-Rh/SiO<sub>2</sub> as compared with nano-TPBpy-Rh and nano-TPTTA is due to the less extended conjugated structure of the thin layer COFs on SiO<sub>2</sub> [37,47]. The band gap of TPTTA<sub>5</sub>@TPBpy<sub>y</sub>-Rh/SiO<sub>2</sub> calculated by Tauc plots was narrower than that of TPTTA<sub>x</sub>/SiO<sub>2</sub>, signifying the good light absorption property of these samples (Fig. S13 and S14). The conduction band minimum (CBM) of TPTTA<sub>5</sub>@TPBpy<sub>y</sub>-Rh/SiO<sub>2</sub> and nano-TPBpy-Rh was measured by Mott-Schottky curves at different frequencies (Fig. 3b-c, S15). All TPTTA<sub>5</sub>@TPBpy<sub>y</sub>-Rh/SiO<sub>2</sub> samples have positive slope of the obtained C<sup>-2</sup> value which revealed the n-type behavior of the samples. The CBM for TPTTA<sub>5</sub>@TPBpy<sub>y</sub>-Rh/SiO<sub>2</sub> was about -0.85 V versus SCE, which was more negative than that of TPBpy-Rh (-0.63 V vs SCE) and more positive than that of TPTTA (-1.27 V vs SCE) [37], indicating the possibility for the transfer of photogenerated electrons from TPTTA to TPBpy-Rh and finally to NAD<sup>+</sup> (Fig. 3d) [48,49]. To further confirm the electron transfer direction, the differential charge density of the interface between TPTTA and TPBpy-Rh was calculated with density functional theory (DFT) method (Fig. S16). The turquoise and yellow regions show the charge transfer from TPTTA to TPBpy-Rh, and the total charge transfer from TPTTA to TPBpy-Rh is 0.04 e<sup>-</sup>.

From electrochemical impedance spectroscopy (EIS) plots, the arc radius of TPTTA<sub>5</sub>@TPBpy<sub>y</sub>-Rh/SiO<sub>2</sub> gradually became smaller with the content of TPBpy-Rh decreasing, indicating that the thin layer TPBpy-Rh favored the good conductivity (Fig. 3e). The lower resistance of TPTTA<sub>5</sub>@TPBpy<sub>0.5</sub>-Rh/SiO<sub>2</sub> facilitates the electron transfer. TPTTA<sub>5</sub>@TPBpy<sub>y</sub>-Rh/SiO<sub>2</sub> could generate photocurrent under visible light (Fig. 3f), showing their possible application in visible light driven photocatalysis. TPTTA<sub>5</sub>@TPBpy<sub>0.5</sub>-Rh/SiO<sub>2</sub> with higher conductivity afforded higher photocurrent response, testifying the efficient

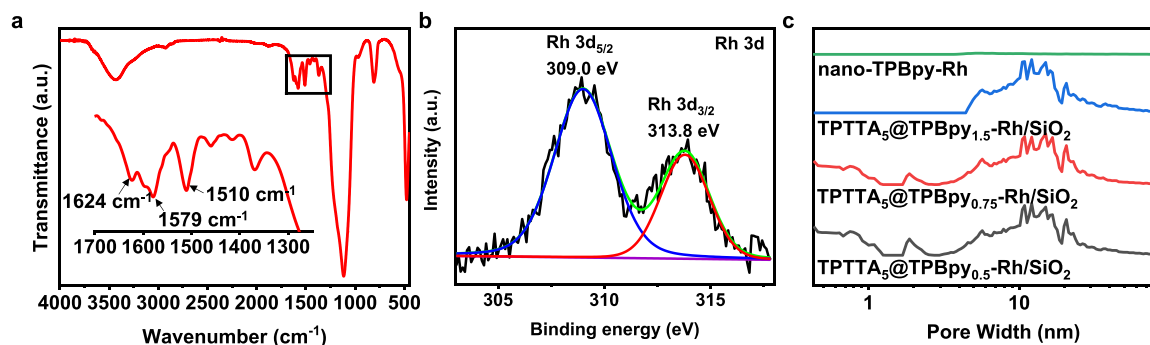


**Fig. 2.** (a) FT-IR spectra, (b) XPS Rh 3d spectrum of TPTTA<sub>5</sub>@TPBpy<sub>0.75</sub>-Rh/SiO<sub>2</sub> and (c) NLDFT pore size distribution curves of nano-TPBpy-Rh and TPTTA<sub>5</sub>@TPBpy<sub>y</sub>/SiO<sub>2</sub>.

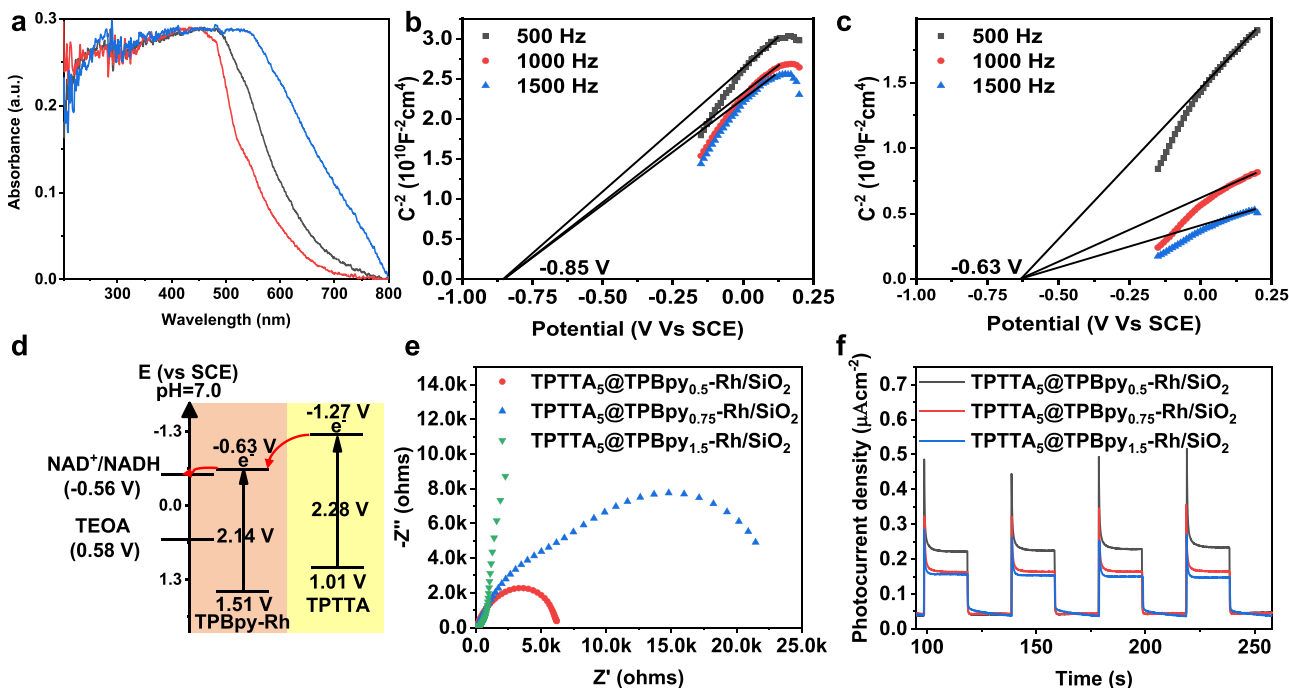


**Fig. 3.** (a) UV–vis diffusion reflectance spectra of  $TPTTA_5/SiO_2$  (red),  $TPTTA_5@TPBpy_{0.75}-Rh/SiO_2$  (black) and nano-TPBpy-Rh (blue), Mott-Schottky plots of (b)  $TPTTA_5@TPBpy_{0.75}-Rh/SiO_2$  and (c) nano-TPBpy-Rh, (d) schematic eletron transfer pathway in  $TPTTA_x@TPBpy_y-Rh/SiO_2$ , (e) EIS of  $TPTTA_5@TPBpy_y-Rh/SiO_2$ , (f) photocurrent density of  $TPTTA_5@TPBpy_y-Rh/SiO_2$ .

separation and migration of photogenerated electrons and holes.

### 3.3. Photocatalytic NADH regeneration

#### 3.3.1. The influence of layer thickness of TPTTA

On the basis of previous report, the band structure of  $TPTTA_x/SiO_2$

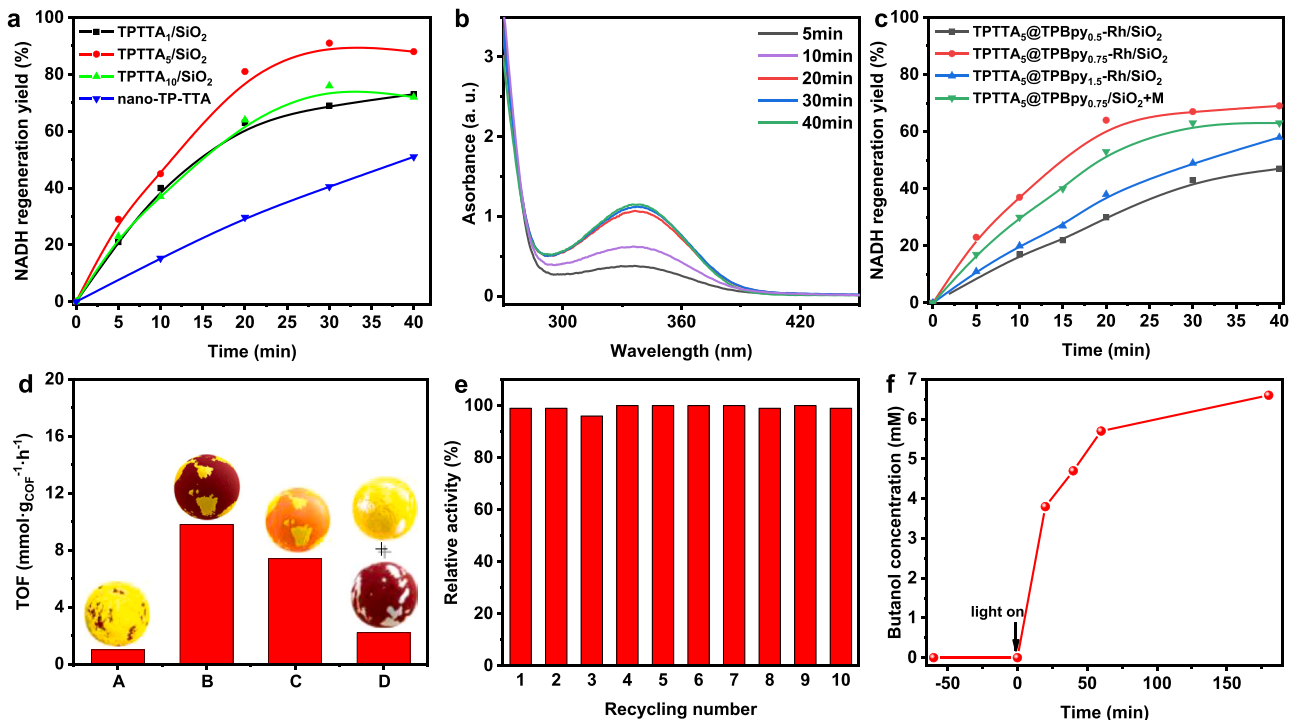


**Fig. 4.** Photocatalytic NADH regeneration reaction profiles of (a)  $TPTTA_x/SiO_2$  and nano-TPTTA, (b) UV-vis spectra of reaction solution for NADH regeneration catalyzed by  $TPTTA_5@TPBpy_{0.75}-Rh/SiO_2$  as a function of reaction time, (c) photocatalytic NADH regeneration reaction profiles of  $TPTTA_5@TPBpy_y-Rh/SiO_2$  and  $TPTTA_5@TPBpy_y/SiO_2$ , (d) the relation of photocatalytic activity and the structure of the composite photocatalyst: (A)  $TPBpy_{0.75}-Rh@TPTTA_5/SiO_2$ , (B)  $TPTTA_5@TPBpy_{0.75}-Rh/SiO_2$ , (C)  $TPBpy_{0.75}@TPTTA_5/SiO_2$  (with free M as electron mediator), (D) mixture of  $TPTTA_5/SiO_2$  and  $TPBpy_{0.75}-Rh/SiO_2$ , (e) recyclability of  $TPTTA_5/SiO_2$  in photocatalytic NADH regeneration, (f) catalytic production of butanol with photobiocoupled  $TPTTA_5@TPBpy_{0.75}-Rh/SiO_2$  and ADH.

matched well with the NAD<sup>+</sup> reduction [29,37]. Thus, the photocatalytic activity of TPTTA<sub>x</sub>/SiO<sub>2</sub> was tested in photocatalytic NAD<sup>+</sup> reduction with M as electron mediator (Table 1). No NADH could be detected without either the light irradiation or the photocatalyst or the hole sacrificial agent or the M. All TPTTA<sub>x</sub>/SiO<sub>2</sub> samples could catalyze the photocatalytic NAD<sup>+</sup> reduction to afford NADH under visible light irradiation with triethanolamine (TEOA) as hole sacrificial agent and M as electron mediator, which was confirmed by the appearance of the characteristic absorption band of NADH at 338 nm in the UV-vis spectrum of the reaction solution (Fig. S17). The band intensity of NADH increased gradually with the extension of reaction time. The reaction profiles showed that TPTTA<sub>5</sub>/SiO<sub>2</sub> afforded larger amounts of NADH than other two TPTTA<sub>x</sub>/SiO<sub>2</sub> and nano-TPTTA COF (Fig. 4a). In 30 min, TPTTA<sub>5</sub>/SiO<sub>2</sub> afforded 91% yield, while TPTTA<sub>1</sub>/SiO<sub>2</sub> and TPTTA<sub>10</sub>/SiO<sub>2</sub> gave moderate yield (69% and 76%), and only 51% yield was achieved with nano-TPTTA COF. The TOF of TPTTA<sub>1</sub>/SiO<sub>2</sub> normalized with TPTTA content is 55.6 mmol·g<sub>COF</sub><sup>-1</sup>·h<sup>-1</sup>, 62 times as much as that of nano-TPTTA COF. The TOF increased as the TPTTA content decreasing, showing the significant influence of the layer thickness of COFs on the photocatalytic activity. This is consistence with our previous report that the H<sub>2</sub> production rate is enormously increased by decreasing the thickness of TPTTA COF to a near-single layer in photocatalytic hydrogen evolution reaction [37]. The high activity of TPTTA<sub>5</sub>/SiO<sub>2</sub> may be ascribed with the combined effect of the charge separation efficiency and the contact between photoactive TPTTA and homogeneous M.

### 3.3.2. The NADH regeneration using photocatalysts with immobilized electron mediator

Considering the high activity of TPTTA<sub>5</sub>/SiO<sub>2</sub> in NAD<sup>+</sup> reduction, M was immobilized on TPTTA<sub>5</sub>/SiO<sub>2</sub> using sequential deposition mentioned above. To our delight, TPTTA<sub>5</sub>@TPBpy<sub>x</sub>-Rh/SiO<sub>2</sub> could smoothly catalyze the NAD<sup>+</sup> reduction with TEOA as hole sacrificial reagent under visible light as evidenced by the appearance of UV-vis absorption band at 338 nm assigned to NADH (Fig. 4b). To identify the efficiency of immobilized M, the reaction solution of TPTTA<sub>5</sub>@TPBpy<sub>0.75</sub>-Rh/SiO<sub>2</sub> was analyzed by enzyme incubation. The enzymatic incubation experiment showed the existence of 69.4% NADH and 27.5% NAD<sup>+</sup> in the solution consistent with the results of UV-vis measurement, showing that all the photo-produced NADH and residue NAD<sup>+</sup> had biological activity (details see SI, Fig. S18). The enzymatic incubation experiment confirmed that neither NAD<sup>+</sup> nor NADH was destroyed during the photocatalytic process, showing the efficiency of the immobilized TPBpy<sub>x</sub>-Rh as electron mediator in facilitating the two electrons coupled proton transfer.

TPTTA<sub>5</sub>@TPBpy<sub>0.75</sub>-Rh/SiO<sub>2</sub> afforded the highest catalytic activity with a NADH yield of 64% in 20 min (Fig. 4c). Considering the inactive nature of TPBpy-Rh COFs in NAD<sup>+</sup> reduction, the TOF was calculated on the basis of TPTTA content, the TOF of TPTTA<sub>5</sub>@TPBpy<sub>0.75</sub>-Rh/SiO<sub>2</sub> reached to 9.8 mmol·g<sub>COF</sub><sup>-1</sup>·h<sup>-1</sup> and follows the order of TPTTA<sub>5</sub>@TPBpy<sub>0.75</sub>-Rh/SiO<sub>2</sub> > TPTTA<sub>5</sub>@TPBpy<sub>0.5</sub>-Rh/SiO<sub>2</sub> > TPTTA<sub>5</sub>@TPBpy<sub>1.5</sub>-Rh/SiO<sub>2</sub>. In comparison with the reported photocatalysts with immobilized M, the activity of TPTTA<sub>5</sub>@TPBpy<sub>0.75</sub>-Rh/SiO<sub>2</sub> was much higher (Table S1). The photoelectric characterizations showed an increased charge separation and migration efficiency with the decreasing of TPBpy-Rh content, while the NADH regeneration activity presented a volcano curve with TPBpy-Rh content. The inconsistency is possibly due to the combined effect of charge separation, surface reaction and diffusion of reactants and products. With comparable textural parameters, the higher TPBpy-Rh content will facilitate the surface reaction but disfavor the electron migration due to the low conductivity of TPBpy. The higher activity of TPTTA<sub>5</sub>@TPBpy<sub>0.75</sub>-Rh/SiO<sub>2</sub> than that of TPTTA<sub>5</sub>@TPBpy<sub>0.5</sub>-Rh/SiO<sub>2</sub> implies that the surface reaction determines the activity of NAD<sup>+</sup> reduction. The low activity of TPTTA<sub>5</sub>@TPBpy<sub>1.5</sub>-Rh/SiO<sub>2</sub> was due to the full coverage of nonporous TPBpy-Rh on TPTTA<sub>5</sub>/SiO<sub>2</sub> surface, which disfavored the mass diffusion

during the catalytic process considering the large molecule of NAD<sup>+</sup>/NADH. With TPTTA<sub>5</sub>@TPBpy<sub>0.75</sub>/SiO<sub>2</sub> as model catalyst, the dosage of M in the photocatalyst was adjusted by using different amounts of [Cp<sup>\*</sup>RhCl<sub>2</sub>]<sub>2</sub> in the coordination process. As the M content reduced from 0.42 wt% to 0.33 wt%, the NADH yield decreased from 69% to 40% with TOF decreasing from 9.8 mmol·g<sub>COF</sub><sup>-1</sup>·h<sup>-1</sup>–2.2 mmol·g<sup>-1</sup>·h<sup>-1</sup>, which is possibly due to the fact that higher amounts of [Cp<sup>\*</sup>RhCl<sub>2</sub>]<sub>2</sub> favored the electron transfer.

The structure of the composite photocatalysts plays an important role in electron transfer direction, which affects the photocatalytic activity. To elucidate the relation of structure and photocatalytic activity, the catalytic activity of the composite photocatalysts with different structure was compared (Fig. 4d). TPBpy<sub>0.75</sub>-Rh@TPTTA<sub>5</sub>/SiO<sub>2</sub> only gave 14% NADH yield in 40 min, much lower than that of TPTTA<sub>5</sub>@TPBpy<sub>0.75</sub>-Rh/SiO<sub>2</sub> (Table 1). The difference between the two photocatalysts is the location of TPTTA and TPBpy. TPTTA<sub>5</sub>@TPBpy<sub>0.75</sub>-Rh/SiO<sub>2</sub> with TPBpy<sub>0.75</sub>-Rh on the outer surface favored the electron transfer to NAD<sup>+</sup>. In contrast, the electron transfer to NAD<sup>+</sup> is unfavorable for TPBpy<sub>0.75</sub>-Rh@TPTTA<sub>5</sub>/SiO<sub>2</sub> with TPBpy<sub>0.75</sub>-Rh in the inner layer due to the diffusion limitation. Notably, TPTTA<sub>5</sub>@TPBpy<sub>0.75</sub>/SiO<sub>2</sub> with free M afforded lower activity than TPTTA<sub>5</sub>@TPBpy<sub>0.75</sub>-Rh/SiO<sub>2</sub> (Table 1, Fig. 4d), suggesting that fixing M on the surface of the photocatalyst can effectively shorten the diffusion length of photogenerated electrons from the photocatalyst to electron mediator to favor the photocatalysis. The physical mixture of TPBpy<sub>0.75</sub>Rh/SiO<sub>2</sub> and TPTTA<sub>5</sub>/SiO<sub>2</sub> only showed 36% NADH yield. The above results suggest the importance of the location and intimate contact of TPTTA and TPBpy-Rh for the efficient transportation of photo-generated electrons to NAD<sup>+</sup>.

The recycling stability of TPTTA<sub>5</sub>/SiO<sub>2</sub> and TPTTA<sub>5</sub>@TPBpy<sub>0.75</sub>-Rh/SiO<sub>2</sub> in photocatalytic NADH regeneration was investigated (Fig. 4e and S19). TPTTA<sub>5</sub>/SiO<sub>2</sub> could well retain the activity for 10 catalytic cycles, indicating the good stability of TPTTA<sub>5</sub>/SiO<sub>2</sub>. TPTTA<sub>5</sub>@TPBpy<sub>0.75</sub>-Rh/SiO<sub>2</sub> could also be stably used for 4 cycles, but the activity declined after the fifth cycle. The FT-IR spectra and the SEM images of used TPTTA<sub>5</sub>/SiO<sub>2</sub> and TPTTA<sub>5</sub>@TPBpy<sub>0.75</sub>-Rh/SiO<sub>2</sub> are almost the same as those of the fresh one (Fig. S20). The ICP result showed that the Rh content of TPTTA<sub>5</sub>@TPBpy<sub>0.75</sub>-Rh/SiO<sub>2</sub> after 5 cycles was 0.38%, corresponding to 10% Rh leaching, which was possibly responsible for the deactivation of TPTTA<sub>5</sub>@TPBpy<sub>0.75</sub>-Rh/SiO<sub>2</sub>.

### 3.3.3. Coupling photocatalytic NADH regeneration and enzymatic reduction

According to previous reports, the light-induced holes and free M in the reaction solution deactivate reductase under illumination by breaking its redox liable amino acid-residues [42]. The TPBpy-Rh in the outer layer of TPTTA<sub>5</sub>@TPBpy<sub>0.75</sub>-Rh/SiO<sub>2</sub> could not only prevent the enzyme from contacting the light-induced holes on TPTTA, but also inhibit the enzyme deactivation. Herein, the photo-enzyme coupling reaction was performed with TPTTA<sub>5</sub>@TPBpy<sub>0.75</sub>-Rh/SiO<sub>2</sub> for photocatalytic NADH regeneration and alcohol dehydrogenase (ADH) for n-butanal reduction with NAD<sup>+</sup> and n-butanal as reactants (Fig. 4f). The control experiment showed that negligible butanol could be detected without either visible light or ADH or TPTTA<sub>5</sub>@TPBpy<sub>0.75</sub>-Rh/SiO<sub>2</sub>, suggesting that all the three are indispensable in photobiocoupled reaction. The coupled system of ADH and TPTTA<sub>5</sub>@TPBpy<sub>0.75</sub>-Rh/SiO<sub>2</sub> continued to produce butanol for at least 180 min, accumulating 6.6 mM butanol. In addition to n-butanal, the benzaldehyde could also be efficiently reduced to benzyl alcohol (0.3 mM benzyl alcohol in 180 min) with TPTTA<sub>5</sub>@TPBpy<sub>0.75</sub>-Rh/SiO<sub>2</sub> and ADH starting from NAD<sup>+</sup>. The above results imply that the TPTTA<sub>5</sub>@TPBpy<sub>0.75</sub>-Rh/SiO<sub>2</sub> showed high compatibility with ADH.

## 4. Conclusion

The efficient photocatalyst for NADH regeneration under visible

light illumination was developed via finely tuning the thickness of COFs layers, which have great influence on the charge separation efficiency, the electron migration and surface reaction. TPTTA<sub>5</sub>/SiO<sub>2</sub> with optimized TPTTA thickness afforded TOF up to 55.6 mmol·g<sub>COF</sub><sup>-1</sup>·h<sup>-1</sup> in photocatalytic NADH regeneration, 62 times higher than that of corresponding nano COFs. After that, the TPTTA<sub>5</sub>@TPBpy-Rh/SiO<sub>2</sub> was prepared by incorporating M (electron mediator) with the deposited TPBpy polymer layer on the TPTTA<sub>5</sub>/SiO<sub>2</sub> using sequential deposition approach. TPTTA<sub>5</sub>@TPBpy<sub>0.75</sub>-Rh/SiO<sub>2</sub> afforded a TOF of 9.8 mmol·g<sub>COF</sub><sup>-1</sup>·h<sup>-1</sup> in photocatalytic NADH regeneration, much higher than most reported photocatalysts. The photocatalyst with immobilized electron mediator was more efficient in electron coupled proton transfer than the physical mixture, which could be assigned to short diffusion length of photogenerated electrons from the photocatalyst to electron mediator. The coupled system of alcohol dehydrogenase and TPTTA<sub>5</sub>@TPBpy<sub>0.75</sub>-Rh/SiO<sub>2</sub> continued to produce butanol for at least 180 min under visible light illumination, implying the high compatibility of this photocatalyst with ADH. The proof-of-principle studies show that regulating charge separation efficiency and surface reaction is an effective strategy to prepare efficient NADH regeneration photocatalyst.

#### CRediT authorship contribution statement

**Jiali Liu:** Prepared and characterized the samples, conducted the photocatalytic reduction and wrote the first manuscript draft. **Xiaomin Ren:** Assisted catalysts preparations. **Chunzhi Li:** Assisted characterizations. **Maodi Wang:** Assisted characterizations. **He Li:** Made recommendations and revised drafts. **Qihua Yang:** Conceived and guided the whole project.

#### Declaration of Competing Interest

The authors declare that they have no known competing financial interests or personal relationships that could have appeared to influence the work reported in this paper.

#### Acknowledgements

This work was supported by the National Natural Science Foundation of China (21733009, 22002162) and the Strategic Priority Research Program of the Chinese Academy of Sciences (XDB17020200).

#### Appendix A. Supporting information

Supplementary data associated with this article can be found in the online version at doi:10.1016/j.apcatb.2022.121314.

#### References

- [1] L. Selles Vidal, C.L. Kelly, P.M. Mordaka, J.T. Heap, Review of NAD(P)H-dependent oxidoreductases: properties, engineering and application, *Biochim. Biophys. Acta Proteins Proteom.* 2018 (1866) 327–347.
- [2] W. Hummel, Large-scale applications of NAD(P)-dependent oxidoreductases: recent developments, *Trends Biotechnol.* 17 (1999) 487–492.
- [3] T. Stehle, Al Claiborne, G.E. Schulz, NADH binding site and catalysis of NADH peroxidase, *Eur. J. Biochem.* 211 (1993) 211–226.
- [4] X. Wang, T. Saba, H.H.P. Yiu, R.F. Howe, J.A. Anderson, J. Shi, Cofactor NAD(P)H regeneration inspired by heterogeneous pathways, *Chem* 2 (2017) 621–654.
- [5] T. Quinto, V. Köhler, Recent trends in biomimetic NADH regeneration, *Top. Catal.* 57 (2014) 321–331.
- [6] J.B. Jones, D.W. Sneddon, W. Higgins, A.J. Lewis, Preparative-scale reductions of cyclic ketones and aldehyde substrates of horse liver alcohol dehydrogenase with *in situ* sodium dithionite recycling of catalytic amounts of NAD, *J. Chem. Soc. Chem. Commun.* (1972) 856–857.
- [7] L. Tensi, A. Macchioni, Extremely fast NADH-regeneration using phosphonic acid as hydride source and iridium-pyridine-2-sulfonamide catalysts, *ACS Catal.* 10 (2020) 7945–7949.
- [8] S. Fukuzumi, Y.-M. Lee, W. Nam, Catalytic recycling of NAD(P)H, *J. Inorg. Biochem.* 199 (2019), 110777.
- [9] X. Wang, H.H.P. Yiu, Heterogeneous catalysis mediated cofactor NADH regeneration for enzymatic reduction, *ACS Catal.* 6 (2016) 1880–1886.
- [10] M. Wang, X. Ren, M. Guo, J. Liu, H. Li, Q. Yang, Chemoselective NADH regeneration: the synergy effect of TiOx and Pt in NAD<sup>+</sup> Hydrogenation, *ACS Sustain. Chem. Eng.* 9 (2021) 6499–6506.
- [11] T. Saba, J. Li, J.W.H. Burnett, R.F. Howe, P.N. Kechagiopoulos, X. Wang, NADH regeneration: a case study of Pt-catalyzed NAD<sup>+</sup> reduction with H<sub>2</sub>, *ACS Catal.* 11 (2021) 283–289.
- [12] F. Hollmann, I.W.C.E. Arends, D. Holtmann, *Enzym. Reduct. Chem.* 13 (2011) 2285–2313.
- [13] C. Kohlmann, W. Märkle, S. Lütz, Electroenzymatic synthesis, *J. Mol. Catal. B Enzym.* 51 (2008) 57–72.
- [14] M. Yuan, M.J. Kummer, R.D. Milton, T. Quah, S.D. Minteer, Efficient NADH regeneration by a redox polymer-immobilized enzymatic system, *ACS Catal.* 9 (2019) 5486–5495.
- [15] K. Xu, A. Chatzitakis, P.H. Backe, Q. Ruan, J. Tang, F. Rise, M. Bjørås, T. Norby, *In situ* cofactor regeneration enables selective CO<sub>2</sub> reduction in a stable and efficient enzymatic photoelectrochemical cell, *Appl. Catal. B Environ.* 296 (2021), 120349.
- [16] W. Jones, J.W.H. Burnett, J. Shi, R.F. Howe, X. Wang, Improving photocatalytic energy conversion via NAD(P)H, *Joule* 4 (2020) 2055–2059.
- [17] Y. Zhang, Y. Zhao, R. Li, J. Liu, Bioinspired NADH regeneration based on conjugated photocatalytic systems, *Sol. RRL* 5 (2021), 2000339.
- [18] Y.-Z. Wang, Z.-P. Zhao, R.-L. Zhou, W.-F. Liu, Optimization of a photoregeneration system for NADH using pristine TiO<sub>2</sub> as a catalyst, *J. Mol. Catal. B Enzym.* 133 (2016) S188–S193.
- [19] S.H. Lee, J. Ryu, D.H. Nam, C.B. Park, Photoenzymatic synthesis through sustainable NADH regeneration by SiO<sub>2</sub>-supported quantum dots, *Chem. Commun.* 47 (2011) 4643–4645.
- [20] J. Liu, M. Antonietti, Bio-inspired NADH regeneration by carbon nitride photocatalysis using diatom templates, *Energy Environ. Sci.* 6 (2013) 1486–1493.
- [21] Y. Tian, Y. Zhou, Y. Zong, J. Li, N. Yang, M. Zhang, Z. Guo, H. Song, Construction of functionally compartmentalized inorganic photocatalyst-enzyme system via imitating chloroplast for efficient photoreduction of CO<sub>2</sub> to formic acid, *ACS Appl. Mater. Interfaces* 12 (2020) 34795–34805.
- [22] Y. Cheng, J. Shi, Y. Wu, X. Wang, Y. Sun, Z. Cai, Y. Chen, Z. Jiang, Intensifying electron utilization by surface-anchored Rh complex for enhanced nicotinamide cofactor regeneration and photoenzymatic CO<sub>2</sub> reduction, *Research* 2021 (2021), 8175709.
- [23] Y. Chen, P. Li, J. Zhou, C.T. Buru, L. Dordević, P. Li, X. Zhang, M.M. Cetin, J. F. Stoddart, S.I. Stupp, M.R. Wasielewski, O.K. Farha, Integration of enzymes and photosensitizers in a hierarchical mesoporous metal-organic framework for light-driven CO<sub>2</sub> reduction, *J. Am. Chem. Soc.* 142 (2020) 1768–1773.
- [24] Y. Wu, J. Shi, D. Li, S. Zhang, B. Gu, Q. Qiu, Y. Sun, Y. Zhang, Z. Cai, Z. Jiang, Synergy of electron transfer and electron utilization via metal-organic frameworks as an electron buffer tank for nicotinamide regeneration, *ACS Catal.* 10 (2020) 2894–2905.
- [25] Y. Zhao, H. Liu, C. Wu, Z. Zhang, Q. Pan, F. Hu, R. Wang, P. Li, X. Huang, Z. Li, Fully conjugated two-dimensional sp<sup>2</sup>-carbon covalent organic frameworks as artificial photosystem I with high efficiency, *Angew. Chem. Int. Ed.* 58 (2019) 5376–5381.
- [26] Y. Wang, H. Liu, Q. Pan, C. Wu, W. Hao, J. Xu, R. Chen, J. Liu, Z. Li, Y. Zhao, Construction of fully conjugated covalent organic frameworks via facile linkage conversion for efficient photoenzymatic catalysis, *J. Am. Chem. Soc.* 142 (2020) 5958–5963.
- [27] D. Yadav, A. Kumar, J.Y. Kim, N.-J. Park, J.-O. Baeg, Interfacially synthesized 2D COF thin film photocatalyst: efficient photocatalyst for solar formic acid production from CO<sub>2</sub> and fine chemical synthesis, *J. Mater. Chem. A* 9 (2021) 9573–9580.
- [28] N. Singh, D. Yadav, S.V. Mulay, J.Y. Kim, N.-J. Park, J.-O. Baeg, Band gap engineering in solvchromic 2D covalent organic framework photocatalysts for visible light-driven enhanced solar fuel production from carbon dioxide, *ACS Appl. Mater. Interfaces* 13 (2021) 14122–14131.
- [29] H. Li, J. Liu, M. Wang, X. Ren, C. Li, Y. Ren, Q. Yang, Fabrication of nanoCOF/polyoxometallate composites for photocatalytic NADH regeneration via cascade electron relay, *Sol. RRL* 5 (2021), 2000641.
- [30] H. Wang, H. Wang, Z. Wang, L. Tang, G. Zeng, P. Xu, M. Chen, T. Xiong, C. Zhou, X. Li, D. Huang, Y. Zhu, Z. Wang, J. Tang, Covalent organic framework photocatalysts: structures and applications, *Chem. Soc. Rev.* 49 (2020) 4135–4165.
- [31] S. Tao, D. Jiang, Covalent organic frameworks for energy conversions: current status, challenges, and perspectives, *CCS Chem.* 2 (2020) 2003–2024.
- [32] F. Zhang, H. Hao, X. Dong, X. Li, X. Lang, Olefin-linked covalent organic framework nanotubes based on triazine for selective oxidation of sulfides with O<sub>2</sub> powered by blue light, *Appl. Catal. B Environ.* 305 (2022), 121027.
- [33] X. Li, S. Yang, F. Zhang, L. Zheng, X. Lang, Facile synthesis of 2D covalent organic frameworks for cooperative photocatalysis with TEMPO: the selective aerobic oxidation of benzyl amines, *Appl. Catal. B Environ.* 303 (2022), 120846.
- [34] Y. Xiang, W. Dong, P. Wang, S. Wang, X. Ding, F. Ichihara, Z. Wang, Y. Wada, S. Jin, Y. Weng, H. Chen, J. Ye, Constructing electron delocalization channels in covalent organic frameworks powering CO<sub>2</sub> photoreduction in water, *Appl. Catal. B Environ.* 274 (2020), 119096.
- [35] Y. Huang, P. Du, W.-X. Shi, Y. Wang, S. Yao, Z.-M. Zhang, T.-B. Lu, X. Lu, Filling COFs with bimetallic nanoclusters for CO<sub>2</sub>-to-alcohols conversion with H<sub>2</sub>O<sub>2</sub> oxidation, *Appl. Catal. B Environ.* 288 (2021), 120001.
- [36] X. Wang, L. Chen, S.Y. Chong, M.A. Little, Y. Wu, W.-H. Zhu, R. Clowes, Y. Yan, M. A. Zwijnenburg, R.S. Sprick, A.I. Cooper, Sulfone-containing covalent organic

frameworks for photocatalytic hydrogen evolution from water, *Nat. Chem.* 10 (2018) 1180–1189.

[37] X. Ren, C. Li, W. Kang, H. Li, N. Ta, S. Ye, L. Hu, X. Wang, C. Li, Q. Yang, Enormous promotion of photocatalytic activity through the use of near-single layer covalent organic frameworks, *CCS Chem.* 3 (2021) 2453–2463.

[38] T. Banerjee, F. Podjaski, J. Kröger, B.P. Biswal, B.V. Lotsch, Polymer photocatalysts for solar-to-chemical energy conversion, *Nat. Rev. Mater.* 6 (2021) 168–190.

[39] H. Liu, C. Li, H. Li, Y. Ren, J. Chen, J. Tang, Q. Yang, Structural engineering of two-dimensional covalent organic frameworks for visible-light-driven organic transformations, *ACS Appl. Mater. Interfaces* 12 (2020) 20354–20365.

[40] H. Li, H. Liu, C. Li, J. Liu, J. Liu, Q. Yang, Micro-scale spatial location engineering of COF-TiO<sub>2</sub> heterojunctions for visible light driven photocatalytic alcohol oxidation, *J. Mater. Chem. A* 8 (2020) 18745–18754.

[41] G. Kumar, R.S. Pillai, N.H. Khan, S. Neogi, Structural engineering in pre-functionalized, imine-based covalent organic framework via anchoring active Ru (II)-complex for visible-light triggered and aerobic cross-coupling of  $\alpha$ -amino esters with indoles, *Appl. Catal. B Environ.* 292 (2021), 120149.

[42] S. Zhang, Y. Zhang, Y. Chen, D. Yang, S. Li, Y. Wu, Y. Sun, Y. Cheng, J. Shi, Z. Jiang, Metal hydride-embedded titania coating to coordinate electron transfer and enzyme protection in photo-enzymatic catalysis, *ACS Catal.* 11 (2020) 476–483.

[43] J. Chen, X. Tao, C. Li, Y. Ma, L. Tao, D. Zheng, J. Zhu, H. Li, R. Li, Q. Yang, Synthesis of bipyridine-based covalent organic frameworks for visible-light-driven photocatalytic water oxidation, *Appl. Catal. B Environ.* 262 (2020), 118271.

[44] W. Zhong, R. Sa, L. Li, Y. He, L. Li, J. Bi, Z. Zhuang, Y. Yu, Z. Zou, A covalent organic framework bearing single Ni sites as a synergistic photocatalyst for selective photoreduction of CO<sub>2</sub> to CO, *J. Am. Chem. Soc.* 141 (2019) 7615–7621.

[45] R. Bu, L. Zhang, X.-Y. Liu, S.-L. Yang, G. Li, E.-Q. Gao, Synthesis and acid-responsive properties of a highly porous vinylene-linked covalent organic framework, *ACS Appl. Mater. Interfaces* 13 (2021) 26431–26440.

[46] D.B. Shinde, H.B. Aiyappa, M. Bhadra, B.P. Biswal, P. Wadge, S. Kandambeth, B. Garai, T. Kundu, S. Kurungot, R. Banerjee, A mechanochemically synthesized covalent organic framework as a proton-conducting solid electrolyte, *J. Mater. Chem. A* 4 (2016) 2682–2690.

[47] Z. Li, K. Geng, T. He, K.T. Tan, N. Huang, Q. Jiang, Y. Nagao, D. Jiang, Editing light emission with stable crystalline covalent organic frameworks via wall surface perturbation, *Angew. Chem. Int. Ed.* 60 (2021) 19419–19427.

[48] M. Masuda, Y. Motoyama, K. Murata, N. Nakamura, H. Ohno, Preparation of an electrode modified with an electropolymerized film as a mediator of NADH oxidation and its application in an ethanol/O<sub>2</sub> biofuel cell, *Electroanalysis* 23 (2011) 2297–2301.

[49] J. Warnan, J. Willkomm, Y. Farré, Y. Pellegrin, M. Boujtita, F. Odobel, E. Reisner, Solar electricity and fuel production with perylene monoimide dye-sensitised TiO<sub>2</sub> in water, *Chem. Sci.* 10 (2019) 2758–2766.